ADVANCED MATERIALS INTERFACES
www.advmatinterfaces.de

$MoSe_2$ Nanosheets Grown on Polydopamine-Derived Porous Fibers: A High-Performance Catalyst for Hydrogen Evolution Reaction

Jiajie Yan, Youfang Zhang, Yunpeng Huang, Yue-E Miao, and Tianxi Liu**

The development of platinum-free electrocatalyst for hydrogen evolution reaction (HER) is highly essential to the large-scale production and application of water splitting devices. Herein, a novel type of molybdenum diselenide decorated porous carbon fiber ($MoSe_2$-PCF) composite has been reported for HER. Notably, the unique mesoporous structure of electrospun polystyrene (PS) fibers is perfectly duplicated via the in situ self-polymerization of dopamine by using PS fibers as the hard template, while porous carbon fibers are formed after the subsequent thermal annealing of polydopamine-coated PS fibers. Thus obtained porous carbon fibers exhibit largely improved surface area which could provide highly conductive framework for electron transport, being an ideal substrate for the decoration of $MoSe_2$. With maximally exposed active edge sites from the perpendicularly orientated $MoSe_2$ nanosheets, the $MoSe_2$-PCF composite exhibits high catalytic activity toward HER, holding great potentials as highly efficient metal-free electrodes for energy related applications.

1. Introduction

As one of the most abundant elements on earth, hydrogen is considered to be an ideal energy carrier to meet the ever increasing global demand for clean and renewable energy.[1] However, the present main technology for large-scale hydrogen production still consumes fossil resources and increases environmental emissions.[2] Exploring low-cost alternative resource and pollution-free fabrication process has attracted much attention in past years while still remains a major challenge. Recently, water splitting offers great promise for clean and efficient production of hydrogen, where the electrocatalyst on the cathode plays a critical role during hydrogen evolution reaction (HER) process.[3] Platinum (Pt)-based metals are considered as the most effective electrocatalytic materials for HER. Nevertheless, the wide-spread practical applications are severely limited by their high cost, scarcity, and weak durability.[4] Therefore, nonprecious catalysts, e.g., transition-metal sulfides,[5] selenides,[6] carbonitrides,[7] phosphides,[8] and nitrides,[9] have been widely investigated as promising candidates to replace Pt-based catalysts for HER.

Molybdenum diselenide ($MoSe_2$), one of the typical transition metal selenides with graphene-like layered structure, has drawn increasing attention recently. Owing to the weak interacting layers of Se–Mo–Se which expose abundant active sites, $MoSe_2$ has been identified as one of the most efficient catalysts for HER.[10] To date, several kinds of $MoSe_2$ nanostructures have been successfully synthesized to show enhanced HER performance.[11] Unfortunately, most of the reported $MoSe_2$ catalysts suffer from severe aggregation and the deletion of favorable charge carriers. To overcome the above limitations, carbon materials with excellent electrical conductivity, such as reduced graphene oxide, carbon nanotubes and porous carbon, have been introduced into $MoSe_2$-based systems for multiple catalytic reactions.[12] In particular, polydopamine (PDA), a kind of biomacromolecules obtained by the self-polymerization of dopamine in a facile environment, has received significant attention for its unique adhesive ability, reduction capability, and conjugation properties.[13] PDA can be directly converted to N-doped conductive carbon by heat treatment. Furthermore, the PDA-derived carbon materials possess similar structure and conductivity to those of multilayer graphene, indicating promising application prospects for energy-related devices.[14] However, very few attempts have been made to explore the potential application of PDA-derived materials as carbon substrate for HER catalysts.

Herein, a facile strategy is reported to fabricate PDA-derived porous carbon fibers decorated with $MoSe_2$ nanosheets as efficient HER catalyst. The synthesis technique is based on a hydrothermal process to grow catalytic active $MoSe_2$ nanosheets on the porous carbon fiber substrate, which is prepared through the self-polymerization of dopamine on electrospun

J. J. Yan, Dr. Y. F. Zhang, Dr. Y. P. Huang, Prof. T. X. Liu
State Key Laboratory of Molecular Engineering of Polymers
Department of Macromolecular Science
Fudan University
220 Handan Road, Shanghai 200433, P. R. China
E-mail: txliu@dhu.edu.cn, txliu@fudan.edu.cn
Dr. Y. E. Miao, Prof. T. X. Liu
State Key Laboratory for Modification of Chemical Fibers and Polymer Materials
College of Materials Science and Engineering
Donghua University
2999 North Renmin Road, Shanghai 201620, P. R. China
E-mail: yuee_miao@dhu.edu.cn

DOI: 10.1002/admi.201600825

polystyrene (PS) fibers followed by a thermal annealing process as previously reported.[15] The PDA-derived porous carbon fiber substrate possesses high specific surface area and electrically conductive pathways due to the sp^2 dominant structure, ensuring proper mass transport of hydrogen and ions via the porous channels. Therefore, the $MoSe_2$ decorated carbon fiber composite exhibits excellent HER activity in acidic media, being a promising Pt-free HER catalyst for potential water electrolysis applications.

2. Results and Discussion

2.1. Morphology and Structure of PDA-Derived Carbon Fibers

The fabrication process of PDA-derived porous carbon fibers is schematically illustrated in **Figure 1**. Initially, PS fibers are prepared via electrospinning using ethanol as the liquid collector (**Figure 2**a), in which process porous structure can be spontaneously introduced into the obtained fibers due to phase separation. Briefly, when PS fibers with partially vaporized solvent, *N,N*-dimethylformamide (DMF) reach the ethanol surface, the solvent quickly dissolves into ethanol while PS cannot be dissolved in ethanol, thus leading to the formation of porous structures in the PS fiber template.[16] As depicted in Figure 2b, plenty of nanosized pores have been clearly observed on the fiber surface while interconnected channels are formed inside the fibers. Moreover, PDA coating can be controllably achieved on PS fiber surface via self-polymerization of dopamine. In contrast to pure PS fibers, the composite fibers after PDA coating exhibit relatively smooth morphology with the homogeneously distributed porous channels completely retained inside the fibers (Figure 2c,d). Afterward, PS@PDA composite fibers with core–shell structures are transformed into porous carbon fibers by thermal annealing at 700 °C. As expected, the carbon fibers derived from PS@PDA composite fibers with proper amount of PDA coating appear to preserve perfect structural integrity, porosity, and core–shell morphology after carbonization (4-porous carbon fiber (PCF), **Figure 3**a,b). Contrarily, the as-obtained carbon fibers with less or excessive PDA coating exhibit destroyed structure (2-PCF, Figure S1a,b, Supporting Information) or PDA agglomerates on the surface (6-PCF, Figure S1c,d, Supporting Information). Figure 3c,d shows the N_2 adsorption–desorption isotherm and pore size distribution plot of the 4-PCF sample. The Brunauer–Emmett–Teller (BET) surface area of the porous fibers reaches up to 378 $m^2 \cdot g^{-1}$ with well-defined mesopores centered at 40–50 nm, which is much higher than that (<100 $m^2 \cdot g^{-1}$) of the previously reported solid fibers.[17] The high surface area and mesoporous architecture of the porous fibers are proposed to be beneficial to electrolyte accessibility and electron transfer,[18] which makes the porous fibers ideal template for the facile construction of carbon/$MoSe_2$ composites.

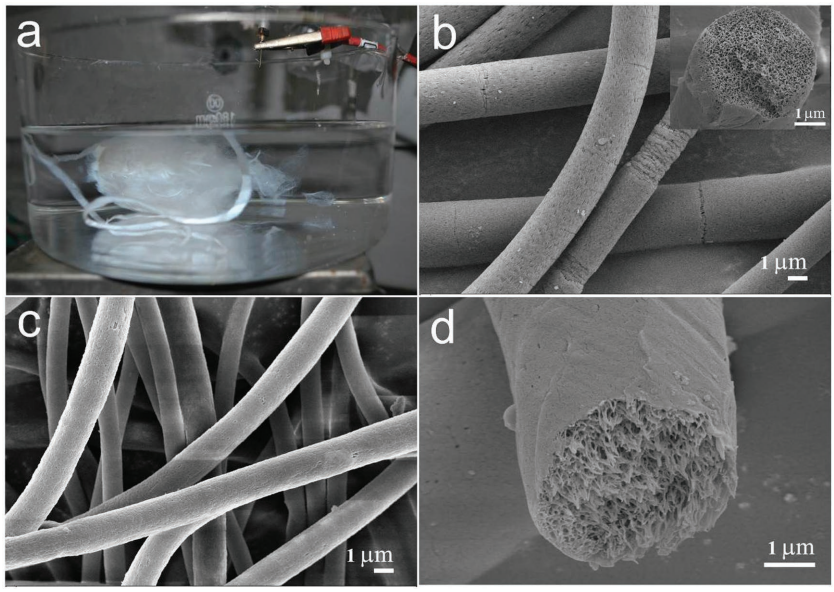

Figure 2. a) Digital photos of the collection setup for porous PS fibers using ethanol as liquid collector. b) SEM image of porous PS fibers, c) PS fibers with PDA coating, and d) the cross-section image of PDA-coated PS fiber.

2.2. Morphology and Structure of $MoSe_2$-PCF Composites

In this work, $MoSe_2$ was synthesized on/within the porous fibers through a hydrothermal process.[12c] **Figure 4**a shows a low-magnification scanning electron microscopy (SEM) image of the as-prepared $MoSe_2$-PCF-2 composite, indicating that the entire surface of the porous carbon fiber is uniformly coated by sheet-like $MoSe_2$ with high density. Close observation of the composite (Figure 4b) reveals that the curled $MoSe_2$ nanosheets are nearly perpendicularly oriented with a diameter of about 100 nm. More excitingly, the representative cross-section image of the composite shows that randomly oriented $MoSe_2$ nanosheets almost cover all the inner surfaces (Figure 4c and Figure S2, Supporting Information), which fully exert the high surface area of the porous carbon substrate. In contrast, pure $MoSe_2$ is quite inaccessible as it tends to form spherical aggregate (Figure 4d), further implying

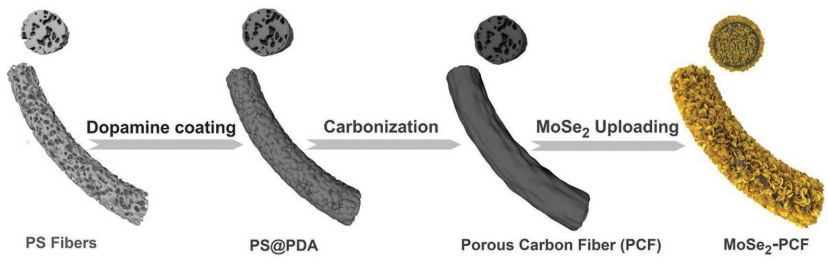

Figure 1. Schematic illustration of the preparation process of $MoSe_2$-PCF composite.

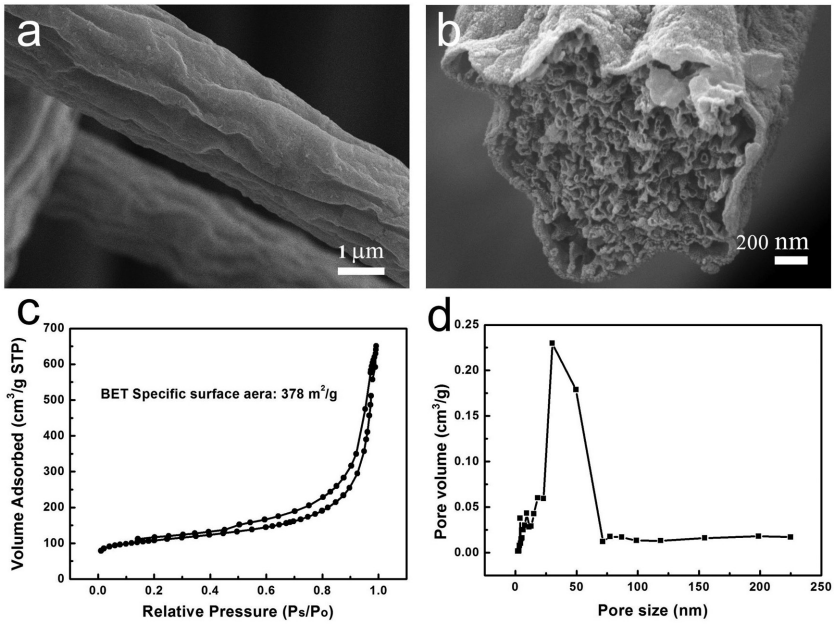

Figure 3. a,b) SEM images of porous carbon fiber (4-PCF). c) Nitrogen adsorption–desorption isotherm at 77 K, and d) the corresponding pore size distribution for 4-PCF sample.

the virtue of employing porous carbon fiber as a novel support for mediating the growth of nanosized $MoSe_2$.[11c]

The crystal structures of as-synthesized carbon fiber, pure $MoSe_2$, and $MoSe_2$-PCF-2 composite were studied using X-ray diffractometer (XRD). As depicted in **Figure 5**, pure carbon fibers show two broad peaks around 25° and 43°, which are indexed to the (002) and (101) reflections of amorphous carbon. After loading certain amount of $MoSe_2$, the $MoSe_2$-PCF composite exhibits four additional diffraction peaks at 2θ = 13.7°, 32.2°, 37.3°, and 56.4°, which are assigned to the (002), (100), (103), and (110) crystal planes of 2H-$MoSe_2$ (JCPDS: 87-2419), revealing the successful growth of $MoSe_2$ on the carbon fiber support. To further determine the elemental composition and valence states of $MoSe_2$-PCF composite, X-ray photoelectron spectroscopy (XPS) analysis was carried out. As expected, the elements of Mo, Se, C, N, and O can be clearly identified from the survey spectrum (Figure 5b). The high-resolution scan of Mo 3d (Figure 5c) shows two major peaks at 229.0 and 232.2 eV assigned to Mo $3d_{5/2}$ and Mo $3d_{3/2}$ orbitals, suggesting the dominance of Mo (IV) in the $MoSe_2$-PCF composite. Besides, small shoulder signals located at 233.6 and 235.8 eV for Mo (VI) oxidation state are observed, which may be ascribed to the slight oxidation of $MoSe_2$.[12b] Figure S3 in the Supporting Information depict the high-resolution scans of Se 3d, and Se 3p electrons, with the well-defined peaks at 55.0 and 56.2 eV for Se $3d_{5/2}$ and Se $3d_{3/2}$, as well as 161.6 and 166.8 eV for Se 3p, signifying the −2 oxidation chemical state of Se.[19] Elemental mapping by energy dispersive X-ray spectroscopy also indicates that Se, Mo, C, and O are uniformly distributed in the $MoSe_2$-PCF composite, with the atomic ratio of Mo and Se collected to be 1/2 (Figure S4, Supporting Information). All these results demonstrate that $MoSe_2$ nanosheets can be successfully deposited on porous carbon fibers through the facile hydrothermal process.

2.3. Electrochemical Characterization of $MoSe_2$-PCF Catalyst

The catalytic activity of $MoSe_2$-PCF-2 composite toward HER was evaluated using a three-electrode electrochemical cell with a sweep rate of 2 $mV \cdot s^{-1}$ in N_2-purged H_2SO_4 solution (aq., 0.5 M). For comparison, pure PCF and $MoSe_2$ were also examined with the polarization curves shown in **Figure 6**. Usually, the onset overpotential and exchange current density are two basic factors to evaluate the catalytic activity of HER catalysts. An optimal catalyst should give the highest current response at the lowest overpotential. It can be observed that $MoSe_2$-PCF-2 composite exhibits a much smaller onset overpotential of about 110 mV versus RHE and achieves a current density of 10 $mA \cdot cm^{-2}$ at the overpotential of 230 mV, whereas pure PCF and $MoSe_2$ show rather poor HER performance. The largely enhanced electrocatalytic activity for $MoSe_2$-PCF can be attributed to the following factors: (1) The porous carbon fiber support not only facilitates the nucleation and growth of $MoSe_2$ with strong interfacial interactions, but also promotes faster electron and

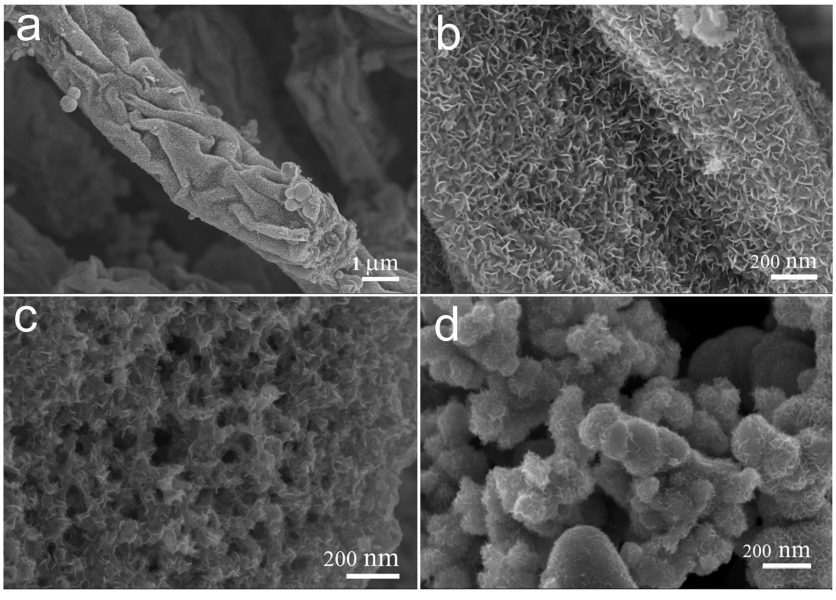

Figure 4. a,b) Low and high-magnification SEM images of $MoSe_2$-PCF-2 composite and c) the corresponding cross-section image. d) SEM image of pure $MoSe_2$.

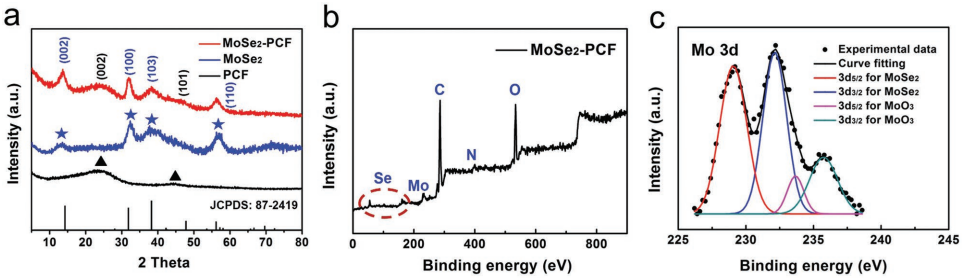

Figure 5. a) XRD patterns of pure PCF, $MoSe_2$, and $MoSe_2$-PCF-2 composite. b) XPS survey spectra of $MoSe_2$-PCF-2 and b) High-resolution spectra of Mo 3d.

ion transport from the less conductive $MoSe_2$ nanosheets to the electrode. (2) $MoSe_2$ nanosheets decorated on fibers with small size and high density can afford abundant accessible edges that could serve as active catalytic sites for HER.

Furthermore, dependence of the HER activity on the loading amount of the active composite has been investigated. As shown in the linear sweep voltammetry (LSV) polarization curves (Figure 6b), the optimal loading amount of $MoSe_2$-PCF-2 composite is 30 μg, which shows a positive onset potential of about 100 mV and a large current density of 17.3 $mA \cdot cm^{-2}$ at the overpotential of 200 mV. It can be easily understood that higher loading amount of the catalyst provides more active sites, thus resulting in higher HER activity. Nevertheless, less material could be electrochemically active due to the limitation of electrolyte diffusion and electron transport when the catalyst film gets too thick. Therefore, a suitable loading amount of the catalyst is critical for achieving excellent HER performance.

A series of $MoSe_2$-PCF composites with varying contents of $MoSe_2$ were fabricated to study the influence of the relative content of $MoSe_2$ on the catalytic activity. As presented in **Figure 7**, SEM images clearly reveal the effect of the precursor concentration on the size and distribution of $MoSe_2$ nanosheets in the composites. At a lower $MoSe_2$ concentration (Figure 7a), insufficient $MoSe_2$ nanosheets are deposited on the fiber surface with some area of the carbon fiber support cannot be fully covered. Further increasing the precursor concentration of $MoSe_2$ can ensure the complete coating of in situ synthesized $MoSe_2$ (Figure 7b,c), with the size reduces initially and then increases according to the crystallization kinetics. However, when the precursor concentration of $MoSe_2$ increases to 20 mg (Figure 7d), excessive $MoSe_2$ nanosheets tend to aggregate on the fiber surface, which may lead to the degradation of the catalytic performance. The observations imply that the lateral growth of $MoSe_2$ nanosheets competes with the early-stage nucleation reaction of $MoSe_2$. Briefly, the concentrations of active hydrazine hydrate and Se play key roles during the crystal growth processes of $MoSe_2$, which facilitate the formation of seeds at the early stage of the reaction under low hydrazine hydrate and Se concentrations while the nucleation and lateral growth of $MoSe_2$ can simultaneously carry out with increased precursor concentrations. Additionally, TGA was also conducted in air atmosphere to quantitatively analyze the $MoSe_2$ content in the composites. As shown in Figure S5 in the Supporting Information, a distinctive weight increment can be observed at 300–400 °C, which is ascribed to the oxidation of $MoSe_2$ according to $2MoSe_2 + 7O_2 = 2MoO_3 + 4SeO_2$, and the residue at 700 °C in air is proved to be MoO_3.[20] Thus, the loading amounts of $MoSe_2$ in $MoSe_2$-PCF-1, $MoSe_2$-PCF-2, $MoSe_2$-PCF-3, and $MoSe_2$-PCF-4 composites are calculated to be 13.7, 26.4, 45.8, and 65.3 wt%, respectively. The pretty high loading amount of $MoSe_2$ may probably provide more active sites for the catalytic reactions.

As mentioned above, the basal edges of $MoSe_2$ have been identified as the active sites for HER, but the overall catalytic activity of this material is limited by the agglomeration and poor electron transport among the domains of $MoSe_2$ nanosheets. Therefore, porous carbon fibers with high surface area are employed as the support to overcome the limited electron–proton transport and maximize the exposed active sites of $MoSe_2$ nanosheets (**Figure 8**a). The polarization curves of $MoSe_2$-PCF composites with different loading amounts of $MoSe_2$ are presented in Figure 8b. It could be observed that $MoSe_2$-PCF-1, $MoSe_2$-PCF-2, and $MoSe_2$-PCF-4 samples exhibit low onset potential of about 120, 100, and 110 mV, respectively,

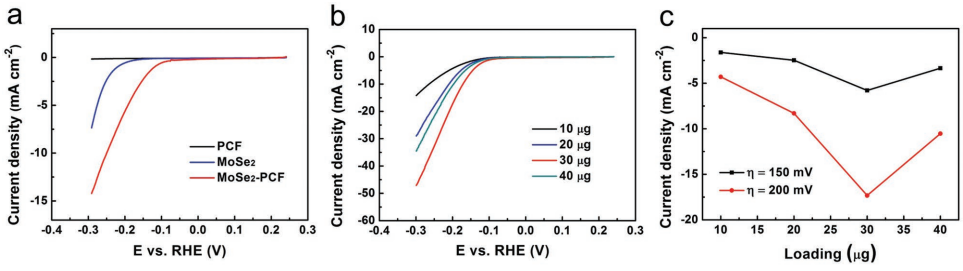

Figure 6. a) LSV polarization curves for pure PCF, $MoSe_2$, and $MoSe_2$-PCF-2 catalysts in 0.5 M H_2SO_4 at a scan rate of 2 $mV \cdot s^{-1}$. b) LSV polarization curves for $MoSe_2$-PCF-2 composite modified GCE under different loading amounts and c) corresponding current densities at overpotentials of 150 and 200 mV.

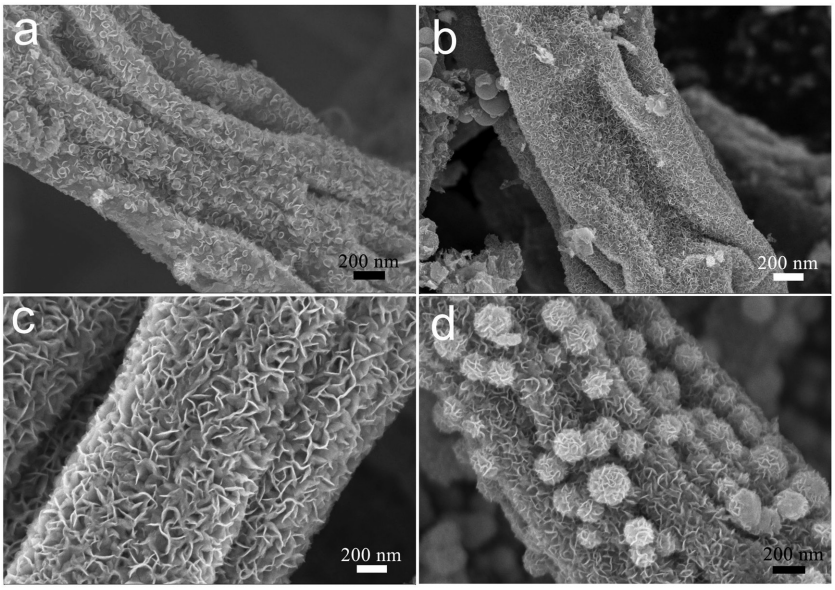

Figure 7. SEM images of a) $MoSe_2$-PCF-1, b) $MoSe_2$-PCF-2, c) $MoSe_2$-PCF-3, and d) $MoSe_2$-PCF-4 composites.

while $MoSe_2$-PCF-3 shows more positive onset potential of about 70 mV. Besides, $MoSe_2$-PCF-3 manifests higher current density over the others at the same potential. Possible reasons for different HER catalytic activity can be deduced from the BET analyses (Figure 8c) and morphological difference (Figure 7). It can be observed that $MoSe_2$-PCF-1, $MoSe_2$-PCF-2, and $MoSe_2$-PCF-3 composites show relatively high specific surface areas of 342, 330, and 323 $m^2 \cdot g^{-1}$, respectively, whereas the $MoSe_2$-PCF-4 composite shows a reduced surface area of 215 $m^2 \cdot g^{-1}$ due to the overloaded $MoSe_2$ aggregates. It is no doubt that the $MoSe_2$-PCF-3 catalyst with both high loading amount and uniform distribution of $MoSe_2$ shows better HER performance than other composites. Notably, the $MoSe_2$-PCF-3 composite displays a small difference of about 40 mV in the onset potential relative to the commercial Pt/C catalyst, which is also competitive to many other previously reported MoS_2- or $MoSe_2$-based HER catalysts (Figure S6, Supporting Information). To further evaluate the intrinsic activity of the composite catalyst, Tafel plots of $MoSe_2$-PCF-3 composite and Pt/C catalyst derived from the corresponding polarization data are shown in Figure 8d, where the linear portions are fit to the Tafel equation ($h = b \log j + a$, where j is the current density and b is the Tafel slope), yielding Tafel slopes of about 65 and 30 $mV \cdot dec^{-1}$ for $MoSe_2$-PCF-3 composite and Pt/C, respectively. For practical applications, a smaller Tafel slope is advantageous, as it requires a lower applied overpotential to generate the required current. Thus, the Tafel slope of 65 $mV \cdot dec^{-1}$ for $MoSe_2$-PCF-3 compares favorably to other non-Pt catalysts, which also suggests that the hydrogen evolution reaction proceeds via a Volmer–Heyrovsky mechanism with the electrochemical desorption process as rate-limiting step.[21]

The HER kinetics of the catalysts at the electrode–electrolyte interface are further investigated by electrochemical impedance spectroscopy (tested at –0.2 V vs RHE). The inset of Figure 8e shows the equivalent circuit model where R_s represents the series resistance, R_{ct} is the charge transfer resistance, and CPE indicates the constant phase element. Obviously, the R_{ct} and R_s of the $MoSe_2$-PCF-3 composite are much lower than those of pure $MoSe_2$, suggesting that the porous carbon fibers with large surface area not only provide highly efficient electron transport but also can help the uniform distribution of $MoSe_2$ nanosheets.[22] Figure 8f and Figure S7 in the Supporting Information show the long-term stability of $MoSe_2$-PCF-3 composite, which is another important concern for a good electrocatalyst. It can be observed that the cathodic current of the catalyst has no obvious deterioration after 1000 cycles. The considerably good catalytic durability of $MoSe_2$-PCF composite can be attributed to the tight binding between active $MoSe_2$ and the porous carbon fiber substrate, further confirming the rational design of the composite as a high-performance HER catalyst.

3. Conclusion

In summary, an efficient and stable carbon/$MoSe_2$ composite electrocatalyst has been developed for HER through the facile pyrolysis of PDA-coated PS fibers and subsequent hydrothermal treatment. The as-prepared PDA-derived carbon fibers hold highly conductive framework and nanoscale channels as well as highly textured surface which facilitate the uniform nucleation and growth of $MoSe_2$ nanosheets. Owing to the synergistic effects of the highly dispersive $MoSe_2$ nanosheets and porous carbon fiber substrate, the optimized $MoSe_2$-PCF catalyst shows remarkable HER activity with a small onset potential of about 70 mV, a low Tafel slope of 65 $mV \cdot dec^{-1}$, and long-term stability in acidic media, which compares favorably to those previously reported nonprecious metal catalysts. Therefore, the $MoSe_2$-PCF composite catalyst is believed to be a promising material for water splitting while the effective strategy might be extended to construct other high-performance composite electrodes for energy-related applications.

4. Experimental Section

Chemicals and Reagents: Polystyrene ($M_w \approx 25\,000$), dopamine hydrochloride (98%), tris(hydroxymethyl)aminomethane (Tris, 99%), tris(hydroxymethyl)aminomethane hydrochloride (Tris·HCl, 99%), and selenium powder (Se, 99.99%) were purchased from Sigma-Aldrich Chem. Co. and used without purification. Na_2MoO_4 (99.99%) and hydrazine hydrate ($N_2H_4 \cdot H_2O$, 50 wt% in water) were supplied by Sinopharm Chemical Reagent Co., Ltd. Pt/C catalyst (20 wt% platinum on carbon black) was obtained from Alfa Aesar. All other reagents were of analytical grade and used without further purification.

Preparation of PDA-Coated PS Fibers: PS was dissolved in DMF at a concentration of 20 wt% under vigorous stirring for 12 h. The precursor solution was loaded into a plastic syringe attached with a needle having an inner diameter of 0.5 mm. A jar of ethanol placed under the nozzle within 10 cm was used as the liquid collector to collect porous PS fibers.

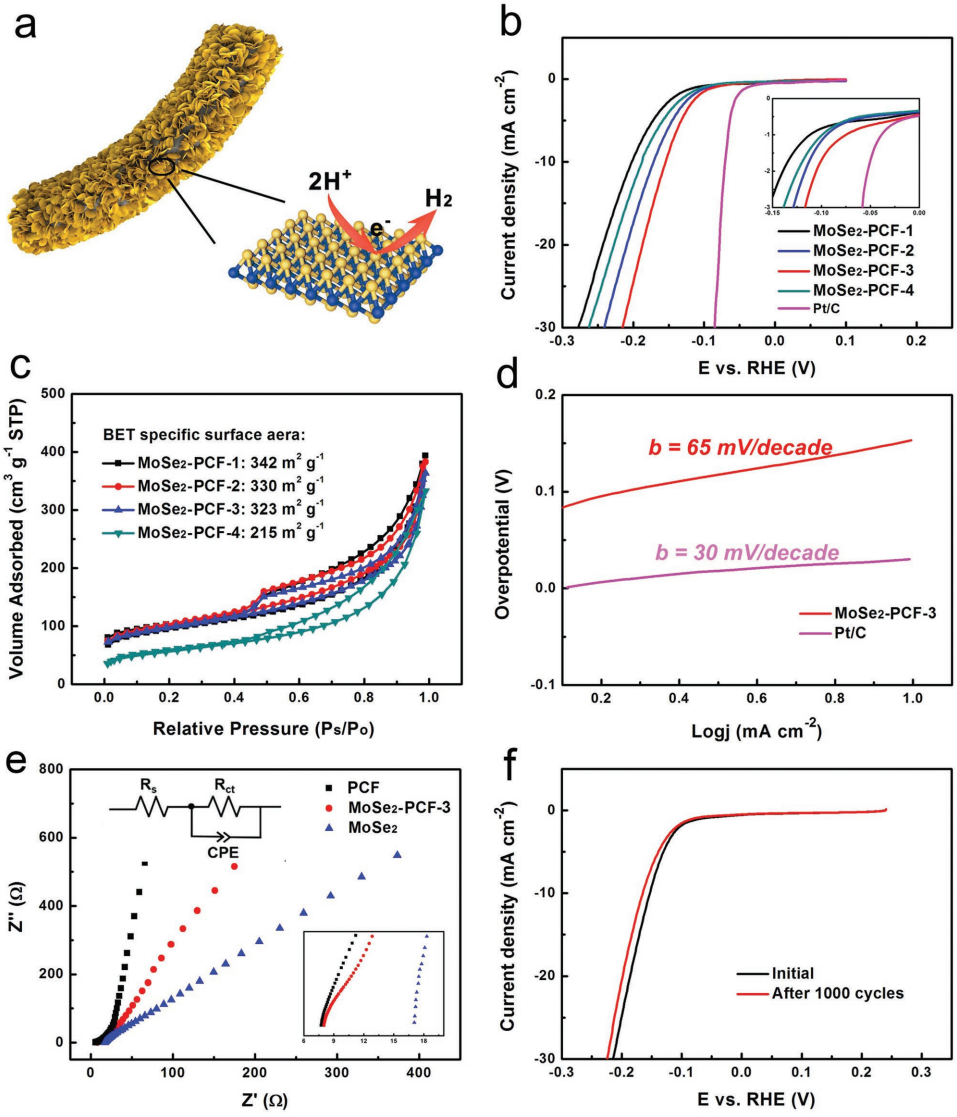

Figure 8. a) Schematic illustration of the nanostructured $MoSe_2$-PCF electrode. The active Mo edge is marked in the magnified crystal structure. Blue sphere: Mo; yellow sphere: Se. b) LSV polarization curves for $MoSe_2$-PCF composites and commercial Pt/C (inset: the corresponding magnified region close to the onset potentials). c) Nitrogen adsorption–desorption isotherms of $MoSe_2$-PCF composites. d) Tafel plots for $MoSe_2$-PCF-3 composite and Pt/C. e) Nyquist plots of PCF, $MoSe_2$, and $MoSe_2$-PCF-3 modified electrodes. f) Durability of the $MoSe_2$-PCF-3 composite.

The flow rate of the solution was set as 2 mL·h^{-1} and voltage applied to the needle tip was fixed at 12 kV. The as-spun PS fibers were then immersed into a tris-buffer solution (10×10^{-3} M, pH = 8.5) dissolved with dopamine hydrochloride at a concentration of 1 mg·mL^{-1} for 2, 4, 6 h, respectively. Then, the fibers were washed by deionized water and overnight dried in a vacuum oven for further use.

Preparation of $MoSe_2$ Decorated Carbon Fiber Composites: According to our previous work,[12c] the synthesis process of the porous carbon fiber loaded with $MoSe_2$ ($MoSe_2$-PCF) was briefly described as follows. Firstly, the precipitated PS fibers with PDA coating were annealed under argon atmosphere at 700 °C for 2 h to remove PS. Thus, PDA-derived PCF were obtained and labeled as 2-PCF, 4-PCF, and 6-PCF according to the immersion time in dopamine solution. The 4-PCF sample was further used as the carbon matrix for in situ growth of $MoSe_2$. In a typical procedure, selenium powder (60 mg) was added into a 100 mL three-neck flask containing 20 mL of hydrazine hydrate, which was kept at 80 °C for 3 h. It should be noticed that hydrazine hydrate could induce neurotoxicity and irreversible eye damage by long-term exposure. Therefore, all the related operations should be conducted in a fume hood with proper protective equipment. The as-prepared PCF fibers were immersed in a H_2SO_4 (98 wt%) bath for 30 min, and thoroughly rinsed with deionized water. Then, 20 mg of the treated 4-PCF fibers were dispersed in 20 mL DMF, together with certain amount of Na_2MoO_4 and hydrazine hydrate-Se (Mo:Se molar ratio fixed at 1:2) for hydrothermal reactions at 180 °C for 10 h. After natural cooling, the product was washed several times with distilled water and overnight dried at 80 °C. Finally, the collected precipitates were annealed in N_2 at 450 °C with a ramp rate of 5 °C min^{-1} for 2 h to yield crystalized $MoSe_2$-PCF composite. In addition, $MoSe_2$-PCF composites with different $MoSe_2$ loading amounts were also synthesized via changing the precursor concentration of $MoSe_2$ (i.e., 5, 10, 15, and 20 mg), which were labeled as $MoSe_2$-PCF-1, $MoSe_2$-PCF-2, $MoSe_2$-PCF-3, and $MoSe_2$-PCF-4, respectively. For comparison, pure $MoSe_2$ in the absence of PCF fibers was also prepared using the same method.

Characterization: Morphology of the samples was investigated using field-emission scanning electron microscope (Ultra 55, Zeiss). XRD data

were collected using a PANalytical (X'Pert PRO) X-ray diffractometer equipped with Cu Kα radiation (λ = 0.1542 nm). Elemental analysis for carbon, nitrogen, molybdenum, and selenium was examined by XPS with a Thermo Electron IRIS Intrepid II device. Specific surface area and pore size distribution of the samples were measured by nitrogen adsorption–desorption method at 77 K (Micromeritics Tristar ASAP 3000) using BET method. TGA analysis was carried out on a Mettler Toledo TGA1 device under constant air flow with a heating rate of 10 °C min^{-1}. Electrochemical measurements were carried out on CHI 600 electrochemical workstation (Shanghai Chenhua Instrument Co., China) with a conventional three-electrode cell using saturated calomel electrode, platinum wire and glassy carbon electrode (GCE) as the reference electrode, counter electrode, and working electrode, respectively. The working electrode was prepared as reported in the previous work.[15] In brief, the as-synthesized catalyst (10 mg) along with a Nafion solution (5 wt%, 0.1 mL; Sigma-Aldrich) was dispersed in a mixed solvent of water/DMF (1:1, v/v; 5 mL) with the assistance of sonication to form a homogeneous ink. Then, 5 mL of this suspension was transferred onto GCE to be fully dried. The LSV was performed in 0.5 M N_2-saturated H_2SO_4 solution with a scan rate of 2 $mV \cdot s^{-1}$ and all polarization curves were not corrected for IR loss. AC impedance measurements were carried out from 10^{-2} to 10^6 Hz with an AC amplitude of 5 mV.

Supporting Information

Supporting Information is available from the Wiley Online Library or from the author.

Acknowledgements

The authors are grateful for the financial support from the National Natural Science Foundation of China (51373037, 51433001).

Received: August 24, 2016
Revised: September 21, 2016
Published online: December 5, 2016

[1] a) A. C. Dillon, K. M. Jones, T. A. Bekkedahl, C. H. Kiang, D. S. Bethune, M. J. Heben, *Nature* **1997**, *386*, 377; b) S. Dunn, *Int. J. Hydrogen Energy* **2002**, *27*, 235; c) J. T. Zhang, Z. H. Zhao, Z. H. Xia, L. L. Dai, *Nat. Nanotechnol.* **2015**, *10*, 444; d) Y. Zhong, X. H. Xia, F. Shi, J. Y. Zhan, J. P. Tu, H. J. Fan, *Adv. Sci.* **2016**, *3*, 1500286.

[2] a) Q. Lu, G. S. Hutchings, W. T. Yu, Y. Zhou, R. V. Forest, R. Z. Tao, J. Rosen, B. T. Yonemoto, Z. Y. Cao, H. M. Zheng, J. Q. Xiao, F. Qiao, J. G. Chen, *Nat. Commun.* **2015**, *6*, 6567; b) S. Han, Y. L. Feng, F. Zhang, C. Q. Yang, Z. Q. Yao, W. X. Zhao, F. Qiu, L. Y. Yang, Y. F. Yao, X. D. Zhuang, X. L. Feng, *Adv. Funct. Mater.* **2015**, *25*, 3899.

[3] a) Y. Jiao, Y. Zheng, M. Jaroniec, S. Z. Qiao, *Chem. Soc. Rev.* **2015**, *44*, 2060; b) X. X. Zou, Y. Zhang, *Chem. Soc. Rev.* **2015**, *44*, 5148; c) C. Y. Ling, L. Shi, Y. X. Ouyang, Q. Chen, J. L. Wang, *Adv. Sci.* **2016**, *3*, 160018.

[4] a) C. G. Morales-Guio, L. A. Stern, X. L. Hu, *Chem. Soc. Rev.* **2014**, *43*, 6555; b) H. W. Liang, S. Brüller, R. H. Dong, J. Zhang, X. L. Feng, K. Müllen, *Nat. Commun.* **2015**, *6*, 7992; c) S. F. Xie, Q. C. Xu, X. Q. Huang, *ChemCatChem* **2016**, *8*, 480.

[5] a) Y. Yan, B. Y. Xia, Z. C. Xu, X. Wang, *ACS Catal.* **2014**, *4*, 1693; b) M. Barawi, I. J. Ferrer, J. R. Ares, C. Sanchez, *ACS Appl. Mater. Interfaces* **2014**, *6*, 20544; c) J. B. Ding, Y. Zhou, Y. G. Li, S. J. Guo, X. Q. Huang, *Chem. Mater.* **2016**, *28*, 2074.

[6] a) I. Tsuji, Y. Shimodaira, H. Kato, H. Kobayashi, A. Kudo, *Chem. Mater.* **2010**, *22*, 1402; b) H. J. Chen, Y. Xie, H. L. Cui, W. Zhao, X. L. Zhu, Y. M. Wang, X. J. Lü, F. Q. Huang, *Chem. Commun.* **2014**, *50*, 4475; c) B. Ni, X. Wang, *Adv. Sci.* **2015**, *2*, 1500085.

[7] a) Y. Zhao, K. Kamiya, K. Hashimoto, S. Nakanishi, *Angew. Chem. Int. Ed.* **2013**, *52*, 13638; b) Y. Zhao, K. Kamiya, K. Hashimoto, S. Nakanishi, *J. Am. Chem. Soc.* **2014**, *137*, 110.

[8] a) Y. Xu, R. Wu, J. F. Zhang, Y. M. Shi, B. Zhang, *Chem. Commun.* **2013**, *49*, 6656; b) T. Tian, L. H. Ai, J. Jiang, *RSC Adv.* **2015**, *5*, 10290; c) Y. Yan, L. Thia, B. Y. Xia, X. M. Ge, Z. L. Liu, A. Fisher, X. Wang, *Adv. Sci.* **2015**, *2*, 1500120.

[9] Y. S. Jun, J. Park, S. U. Lee, A. Thomas, W. H. Hong, G. D. Stucky, *Angew. Chem. Int. Ed.* **2013**, *125*, 11289.

[10] a) Y. F. Shi, C. X. Hua, B. Li, X. P. Fang, C. H. Yao, Y. C. Zhang, Y. S. Hu, Z. X. Wang, L. Q. Chen, D. Y. Zhao, *Adv. Funct. Mater.* **2013**, *23*, 1832; b) F. H. Saadi, A. I. Carim, J. M. Velazquez, J. H. Baricuatro, C. C. L. McCrory, M. P. Soriaga, N. S. Lewis, *ACS Catal.* **2014**, *4*, 2866.

[11] a) Y. J. Zhang, Q. F. Gong, L. Li, H. C. Yang, Y. G. Li, Q. B. Wang, *Nano Res.* **2014**, *8*, 1108; b) X. L. Zhou, J. Jiang, T. Ding, J. J. Zhang, B. C. Pan, J. Zuo, Q. Yang, *Nanoscale* **2014**, *6*, 11046; c) D. Sun, S. M. Feng, M. Terrones, R. E. Schaak, *Chem. Mater.* **2015**, *27*, 3167.

[12] a) H. Tang, K. P. Dou, C. C. Kaun, Q. Kuang, S. H. Yang, *J. Mater. Chem. A* **2014**, *2*, 360; b) L. P. Jia, X. Sun, Y. M. Jiang, S. J. Yu, C. M. Wang, *Adv. Funct. Mater.* **2015**, *25*, 1814; c) Y. P. Huang, H. Y. Lu, H. H. Gu, J. Fu, S. Y. Mo, C. Wei, Y. E. Miao, T. X. Liu, *Nanoscale* **2015**, *7*, 18595.

[13] a) J. J. Wilker, *Nat. Chem. Biol.* **2011**, *7*, 579; b) Z. M. Wang, C. Li, J. L. Xu, K. F. Wang, X. Lu, H. P. Zhang, S. X. Qu, G. M. Zhen, F. Z. Ren, *Chem. Mater.* **2015**, *27*, 848; c) H. Shen, Y. H. Long, X. L. Yang, N. Zhao, J. Xu, *Polym. Int.* **2015**, *64*, 986.

[14] a) R. Liu, S. M. Mahurin, C. Li, R. R. Unocic, J. C. Idrobo, H. J. Gao, S. J. Pennycook, S. Dai, *Angew. Chem. Int. Ed.* **2011**, *50*, 6799; b) J. B. Xi, Y. T. Xia, Y. Y. Xu, J. W. Xiao, S. Wang, *Chem. Commun.* **2015**, *51*, 10479.

[15] J. J. Yan, H. Y. Lu, Y. P. Huang, J. Fu, S. Y. Mo, C. Wei, Y. E. Miao, T. X. Liu, *J. Mater. Chem. A* **2015**, *3*, 23299.

[16] a) J. H. Kong, C. Y. Zhao, Y. F. Wei, S. L. Phua, Y. L. Dong, X. H. Lu, *J. Mater. Chem. A* **2014**, *2*, 15191; b) J. H. Kong, X. Y. Yao, Y. F. Wei, C. Y. Zhao, J. M. Ang, X. H. Lu, *RSC Adv.* **2015**, *5*, 13315.

[17] a) J. Wu, H. W. Park, A. P. Yu, D. Higgins, Z. W. Chen, *J. Phys. Chem. C* **2012**, *116*, 9427; b) S. G. Wang, Z. T. Cui, M. H. Cao, *Chem. Eur. J.* **2014**, *21*, 2165.

[18] a) K. Xiao, L. X. Ding, H. B. Chen, S. Q. Wang, X. H. Lu, H. H. Wang, *J. Mater. Chem. A* **2016**, *4*, 372; b) C. Z. Zhu, H. Li, S. F. Fu, D. Du, Y. H. Lin, *Chem. Soc. Rev.* **2016**, *45*, 517.

[19] C. H. Mu, H. X. Qi, Y. Q. Song, Z. P. Liu, L. X. Ji, J. G. Deng, Y. B. Liao, F. Scarpa, *RSC Adv.* **2016**, *6*, 23.

[20] a) Y. P. Huang, Y. E. Miao, J. Fu, S. Y. Mo, C. Wei, T. X. Liu, *J. Mater. Chem. A* **2015**, *3*, 16263; b) Y. Liu, M. Q. Zhu, D. Chen, *J. Mater. Chem. A* **2015**, *3*, 11857.

[21] a) B. E. Conway, B. V. Tilak, *Electrochim. Acta* **2002**, *47*, 3571; b) J. O. Bockris, I. A. Ammar, A. Huq, *J. Phys. Chem.* **1957**, *61*, 879.

[22] D. Li, Y. P. Wen, J. K. Xu, H. H. He, M. Liu, *Chin. J. Polym. Sci.* **2012**, *30*, 705.

